DC Electric Metamaterial Behaviour in Fused Filament Fabrication Prints with Tuned Interfaces

Alexander Dijkshoorn ⬤, *Graduate Student Member, IEEE*, Thijs Hamstra, Remco Sanders, Stefano Stramigioli ⬤, *Fellow, IEEE*, Gijs Krijnen ⬤, *Senior Member, IEEE*

Robotics and Mechatronics Group, University of Twente, Enschede, the Netherlands

a.p.dijkshoorn@utwente.nl

Abstract—DC Electric metamaterials are interesting for electronics, sensors and actuators by enabling steering of current. In this paper we realize such DC electric metamaterials with Fused Filament Fabrication by tuning the nozzle temperature, bed temperature and extrusion width to achieve anisotropic electrical conduction. Both temperatures influence the magnitude of the contact resistance between printed lines, whereas the extrusion width determines the number of interfaces per unit length. An anisotropic effective medium approximation model is used to analyze the effect of the electrical parameters and is verified with Finite Element (FEM) simulations. Measurements are performed with a setup inspired by the pseudo-Hall effect. Finally, exploiting the anisotropic properties of 3D printed conductors, we present a current concentrator and its operation is demonstrated through IR thermography and voltage measurements.

Index Terms—3D-Printing, Fused Filament Fabrication, Electric Metamaterial, Conductive, Anisotropy, Effective Medium

I. Introduction

3D-PRINTING of electrically conductive materials for sensor [2]–[4] and structural electronics [5], [6] applications by means of Fused Filament Fabrication (FFF) is an upcoming area of research. This method allows for embedding sensors with electronics in objects in one manufacturing step [7], [8]. On the other hand the FFF process introduces anisotropy due to line-wise and layer-wise manufacturing, e.g. giving rise to anisotropic electrical properties due to the contact resistances between lines and layers [9]–[11], where a full understanding of the effect of printing parameters on the anisotropy is still lacking [12]. The printing induced anisotropic properties have e.g. been used for sensing [13], [14], electromagnetic shielding [15] and electrical heating [16]. On the other hand the printing process has been tuned to reduce the anisotropy, e.g. in 3D-printed sensors [17], [18]. The anisotropy can be exploited to obtain metamaterial behaviour in sensors and electronics [19]. Metamaterials can serve sensor purposes by enhancing the sensitivity through concentrating the fields used to measure [20], [21] or by cloaking the sensor to prevent perturbing the to-be-measured field [22]. It has been shown that anisotropic, time-independent DC metamaterials, e.g. for the thermal and electrical domains,

can be realized with layered structures of two materials with dissimilar conductivities [23]–[25]. Furthermore imperfect interfaces between the layers significantly influence the DC metamaterial performance [26], [27], and can be considered equally well for creating the desired performance [28], [29].

Currently, the fabrication of DC electric metamaterials is achieved by creating resistor networks [21], [30], [31] and by stacking or merging thin layers of materials [22], [23], [32]. To solve the challenge of rapid and cost-effective fabrication, recently a laser-induced-graphene method was introduced for thermal metamaterials [33]. In this respect 3D-printing, and especially FFF with its anisotropy due to the structured materials it produces, can offer advantages in terms of costs, geometric freedom, available materials, lead time and embedding when used as fabrication method for DC metamaterials [34]–[37]. Furthermore the infill pattern of (multi-material) FFF with its sub-millimeter resolution is ideally suited to print the repeating, layered structures required for DC metamaterials [34].

Since realizing metamaterials with FFF is expected to offer an additional tool in the design toolbox for 3D-printing of sensors and conductors, this work studies the fabrication of DC electric metamaterials by means of Fused Filament Fabrication. An effective medium model is introduced to explain the metamaterial performance, the effect of several printing parameters on the anisotropic electrical conduction is measured and the findings are used to demonstrate a 3D-printed DC electric metamaterial concentrator. The following sections present thetheory and compare modeling, simulations and experimental data to demonstrate the role of the printing parameters and the metamaterial operation.
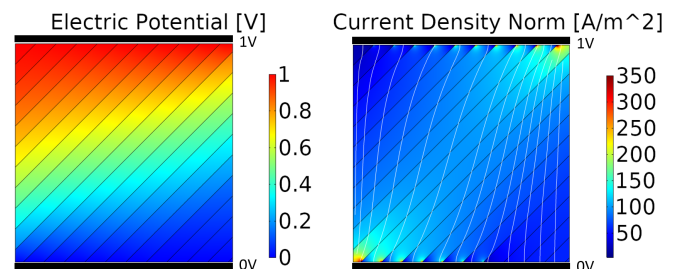

Fig. 1: FEM simulation of a 3D-printed layer, showing a skewed voltage distribution (left) and an skewed current density norm distribution (right) due to contact resistance between lines. The current density plot contains the streamlines in white to show the current density paths.

II. Theory

Metamaterials can be defined as intentionally designed materials with an, often periodic, artificial structure. The properties are dictated to a large extend by the structure instead of only by the properties of the base material [34], [35]. The periodic structure should also be significantly smaller than the wavelength, which is not a problem for DC (non-resonant) electromagnetic metamaterials since the wavelength diverges at zero frequency [38].

In this study single 3D-printed sheets with a $45°$ infill pattern are studied, of which a Finite Element Method (FEM) simulation with skewed voltage distribution is shown in fig. 1.a. A single material with contact resistance between the printed lines is used to create the anisotropic conduction, instead of the standard method of using two materials with different resistivities. These tiles can be combined in different patterns to achieve different functionalities, e.g. to cloak, to concentrate, to diffuse [25], [39].

Modeling shows that both the orientation of the layers and an additional tuning parameter based on the material properties can be used to change the direction and magnitude of the electric field for an infinite sheet with dual material layers [40]. In the present research the anisotropy is determined by the contact resistance instead of by dual materials. The prints have an in-line resistivity of ρ in $\Omega\,\mathrm{m}$ and a homogenized resistivity of $\rho + \sigma/W$ perpendicular to the printed lines, with σ in $\Omega\,\mathrm{m}^2$ being the contact resistivity and W the line width. For large σ the current density mainly follows the infill direction, yielding a skewed voltage distribution like in fig. 1.a. The relative effect of the interfaces can be given by the anisotropy ratio, defined as the ratio of resistivities in the direction along and the direction normal to the printed lines [19]:

$$\Gamma := \frac{\rho}{\rho + \sigma/W} = \frac{1}{1 + \frac{\sigma/W}{\rho}} = \frac{1}{1 + \beta} \qquad (1)$$

Where $\beta := (\sigma/W)/\rho$ is introduced as shorthand notation of the ratio between contact and bulk resistivity. In case of ideal isotropic conduction $\Gamma = 1$ and for significant anisotropy, with DC electric metamaterial properties, $\Gamma \ll 1$ (which corresponds to $\beta = 0$ and $\beta \gg 1$ respectively).

To obtain electrical conduction with FFF, usually conductive-polymer composites are used, e.g. a polymer filled with nano-particles like carbon black [12]. It is expected that the printing parameters can be tuned to affect the fusion and therefore the contact resistivity σ and, hence, Γ. The contact resistance is likely accounted for by (a combination of) voids, improper fusion, nanoparticle alignment and the distribution of conductive nanoparticles [11], [12], [41]. For a given material the nozzle temperature T_{noz} and the environment or bed temperature T_{bed} are crucial in the bond formation between lines [42], [43]. Higher temperatures in general give lower total resistance for 3D-prints [11], [44]. Furthermore the line or extrusion width W_{ext} determines the number of interfaces for a fixed sample size, and increasing it is shown to minimize the total resistance in 3D-prints [9], [11] (W_{ext} specifies the line width for the 3D-printing process, whereas line width W in the model applies to any layered

structure). Therefore the printing parameters under study are T_{noz}, T_{bed} and W_{ext}. First a model is introduced to get a better understanding of the effect of ρ, σ and W_{ext}.

A. Model

The redirection of the electric field component with respect to an applied current is already modeled for infinite sheets of periodic, dual material multilayer structures by Tarkhanyan et al. by means of approximating the effective resistivity tensor as an anisotropic, homogeneous medium [40]. We extend this effective medium approximation (EMA) for the case of resistive interfaces, where we solve the Laplace equation on a finite, rectangular geometry with the effective resistivity tensor based on the work of Moelter et al. with nonorthogonal basis functions [45]. This solution can then be used to predict and interpret measurements.
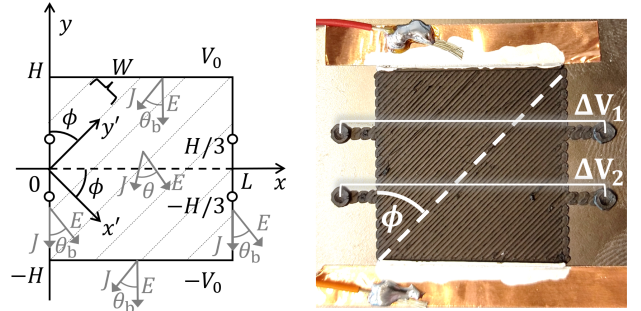

Fig. 2: The important dimensions of the layered composite with the printed lines rotated over angle ϕ, showing redirection angle θ of the electric field $\mathbf{E}$ with respect to the applied current density $\mathbf{J}$ and constant θ_{b} at the borders (left), adapted from [45]. The 3D-printed sample with an infill angle of $\phi = 45°$, contacts made of copper tape with silver paint and two pairs of probing points to measure the skewed voltage due to anisotropy at two positions, ΔV_1 and ΔV_2 (right).

Fig. 2 shows the structure of aligned track elements (traxels) of width W with bulk resistivity ρ and interfaces with contact resistivity σ under an angle ϕ. For an applied DC electric current density $\mathbf{J}$ and the resistivity tensor $\hat{\rho}_{\mathrm{eff}}$ the electric field becomes [40]:

$$\mathbf{E} = \hat{\rho}_{\mathrm{eff}}\mathbf{J} \qquad (2)$$

In the unrotated coordinate frame $x'y'$, the resistivity tensor is expressed by:

$$\hat{\rho}'_{\mathrm{eff}} = \begin{bmatrix} \rho'_{xx} & 0 \\ 0 & \rho'_{yy} \end{bmatrix} = \begin{bmatrix} \rho + \sigma/W & 0 \\ 0 & \rho \end{bmatrix} \qquad (3)$$

Where the separate components in x' and y'-direction can be derived by averaging the resistivity components. To find the electric field in the rotated xy coordinate frame, $\hat{\rho}'_{\mathrm{eff}}$ has to be rotated by ϕ with rotation matrix $\hat{A}$:

$$\begin{bmatrix} E_x \\ E_y \end{bmatrix} = \hat{A}\hat{\rho}'_{\mathrm{eff}}\hat{A}^{-1} \begin{bmatrix} J_x \\ J_y \end{bmatrix} = \hat{\rho}_{\mathrm{eff}} \begin{bmatrix} J_x \\ J_y \end{bmatrix} = \begin{bmatrix} \rho_{xx} & \rho_{xy} \\ \rho_{yx} & \rho_{yy} \end{bmatrix} \begin{bmatrix} J_x \\ J_y \end{bmatrix} =$$
$$\begin{bmatrix} \rho'_{xx}\cos^2(\phi) + \rho'_{yy}\sin^2(\phi) & (\rho'_{yy} - \rho'_{xx})\sin(\phi)\cos(\phi) \\ (\rho'_{yy} - \rho'_{xx})\sin(\phi)\cos(\phi) & \rho'_{yy}\cos^2(\phi) + \rho'_{xx}\sin^2(\phi) \end{bmatrix} \begin{bmatrix} J_x \\ J_y \end{bmatrix} \qquad (4)$$

This system of equations can be solved to find the expression for **J**, with conductivity tensor $\hat{\kappa}_{\text{eff}}$ (introduced as $\hat{\kappa}_{\text{eff}}$ to prevent confusion with the contact resistivity σ):

$$\begin{bmatrix} J_x \\ J_y \end{bmatrix} = \hat{\rho}_{\text{eff}}^{-1} \begin{bmatrix} E_x \\ E_y \end{bmatrix} = \hat{\kappa}_{\text{eff}} \begin{bmatrix} E_x \\ E_y \end{bmatrix} =$$
$$\frac{1}{\rho_{xx}\rho_{yy} - \rho_{xy}\rho_{yx}} \begin{bmatrix} \rho_{yy} & -\rho_{yx} \\ -\rho_{xy} & \rho_{xx} \end{bmatrix} \begin{bmatrix} E_x \\ E_y \end{bmatrix} \quad (5)$$

Note that due to the anisotropic resistivity, there exists a transverse electric field and hence a redirection or bending angle θ between the electric field and the current density. Therefore, the current density is not perpendicular to the equipotential lines, as would be the case for isotropic materials. Since no current can go through the edges at $x = 0$ and $x = L$, it must hold that $J_x(0, y) = 0$ and $J_x(L, y) = 0$. This results in the following conditions for the electric field:

$$E_x(0, y) = \rho_{xy} J_y(0, y) = \frac{\rho_{xy}}{\rho_{yy}} E_y(0, y) := \lambda E_y(0, y) \quad (6)$$

$$E_x(L, y) = \rho_{xy} J_y(L, y) = \frac{\rho_{xy}}{\rho_{yy}} E_y(L, y) := \lambda E_y(L, y) \quad (7)$$

where the parameter λ expresses the ratio of the transverse component of the electric field to the vertical component at the left and right hand edge due to the anisotropy:

$$\lambda = \frac{\rho_{xy}}{\rho_{yy}} = \frac{(\rho'_{yy} - \rho'_{xx})\sin(\phi)\cos(\phi)}{\rho'_{yy}\cos^2(\phi) + \rho'_{xx}\sin^2(\phi)} = \frac{-\beta\tan(\phi)}{1 + (1+\beta)\tan^2(\phi)} \quad (8)$$

Where $\beta = \rho'_{xx}/\rho'_{yy} - 1 = (\sigma/W)/\rho$ is the same as in eq. 1. Furthermore the electric field can be expressed in terms of the potential $E_x = -\frac{\partial V}{\partial x}$ and $E_y = -\frac{\partial V}{\partial y}$, yielding the final boundary conditions at the left and right hand-side boundary:

$$\left.\frac{\partial V}{\partial x}\right|_{x=0} = \lambda \left.\frac{\partial V}{\partial y}\right|_{x=0} \quad (9)$$

$$\left.\frac{\partial V}{\partial x}\right|_{x=L} = \lambda \left.\frac{\partial V}{\partial y}\right|_{x=L} \quad (10)$$

This means that all equipotential lines have a slope of λ at the left and right boundary [45]. This slope can be related to the constant redirection angle at the boundaries θ_b through:

$$\tan(\theta_b) = \lambda \quad (11)$$

The conditions for eq. 11 only hold at the boundaries (at the sides as well as at the top and bottom). Hence, redirection angle θ is not constant within an anisotropic sample [46]. Finally the upper and lower boundaries are kept at a constant potential:

$$V(x, H) = V_0 \quad (12)$$

$$V(x, -H) = -V_0 \quad (13)$$

The boundary-value problem can then be complemented by the Laplace equation. For an isotropic, homogeneous material the Laplace equation $\nabla^2 V = 0$ in the region $0 \leq x \leq L$ and $-H \leq y \leq H$ can be solved subject to the above boundary conditions, following the method with nonorthogonal basis functions by Moelter et al. to deal with the unusual boundary conditions [45]. However, in this research an anisotropic medium is present, yielding the anisotropic Laplace equation [47]:

$$\nabla \cdot (\hat{\kappa}_{\text{eff}} \nabla V) = 0 \quad (14)$$

Since the electrical conductivity tensor in anisotropic, homogeneous media is symmetrical, the electric potential field in 2D becomes [47]:

$$\kappa_{xx}\frac{\partial^2 V}{\partial x^2} + 2\kappa_{xy}\frac{\partial^2 V}{\partial x \partial y} + \kappa_{yy}\frac{\partial^2 V}{\partial y^2} = 0 \quad (15)$$

From eq. 4 it follows that $\hat{\rho}_{\text{eff}}$ is symmetric and that $\rho_{xx} = \rho_{yy}$ for $\phi = 45\,\text{deg}$. Through eq. 5 this also holds for $\hat{\kappa}_{\text{eff}}$, yielding: $\lambda = \frac{\rho_{xy}}{\rho_{yy}} = -\frac{\kappa_{xy}}{\kappa_{xx}}$. Hence, eq. 15 can be rewritten as:

$$\frac{\partial^2 V}{\partial x^2} - 2\lambda\frac{\partial^2 V}{\partial x \partial y} + \frac{\partial^2 V}{\partial y^2} = 0 \quad (16)$$

Athanasopoulos et al. work with the same boundary value problem for anisotropic conduction in carbon fibre reinforced plastics (CFRP) and solve this problem numerically [47]. To solve the problem analytically, the term $2\lambda\frac{\partial^2 V}{\partial x \partial y}$ needs to be negligible. This holds in case:

$$|2\lambda| = \left|\frac{2\rho_{xy}}{\rho_{yy}}\right| = \frac{2\sigma/W}{2\rho + \sigma/W} = \frac{\beta}{1 + \beta/2} << 1 \quad (17)$$

This also requires simple geometries with small sense contacts and almost homogeneous current density [48]. So when $\beta << 1$ or $\sigma/W << \rho$ and $\phi = 45\,\text{deg}$ the anisotropic Laplace equation simplifies to the isotropic case and the anisotropy in the material is purely incorporated through the boundary conditions:

$$\left.\frac{\partial^2 V}{\partial x^2}\right|_{\sigma/W << \rho} + \left.\frac{\partial^2 V}{\partial y^2}\right|_{\sigma/W << \rho} \approx 0 \quad (18)$$

Hence, the boundary-value problem is given by eq. 18 in the region $0 \leq x \leq L$ and $-H \leq y \leq H$ subject to eq. 9 and 12. For this case the solution method by Moelter et al. with nonorthogonal basis functions can be followed [45] due to the similarity between the Hall conductivity tensor and the conductivity tensor with a transverse conduction component in eq. 5, yielding the solution for the potential:

$$V(x, y) = \frac{V_0}{H}\left[\lambda\left(x - \frac{L}{2}\right) + y + \sum_{m=1,3,\dots} T_m\left[\cos\left(\frac{m\pi}{L}x\right)\cosh\left(\frac{m\pi}{L}y\right) + \lambda\sin\left(\frac{m\pi}{L}x\right)\sinh\left(\frac{m\pi}{L}y\right)\right]\right.$$
$$\left. + \sum_{n=2,4,\dots} U_n\left[\cos\left(\frac{n\pi}{L}x\right)\sinh\left(\frac{n\pi}{L}y\right) + \lambda\sin\left(\frac{n\pi}{L}x\right)\cosh\left(\frac{n\pi}{L}y\right)\right]\right] \quad (19)$$

Due to the nonorthogonal basis functions that result from boundary conditions in eq. 9, the coefficients T_m and U_n of the series expansion need to be solved iteratively. However, λ is small due to the earlier assumption of $|2\lambda| << 1$, and it is sufficient to approximate the coefficients to the order λ^2 [45]:

$$T_m \approx \frac{4V_0 L\lambda}{\pi^2 H m^2 \cosh(m\pi H/L)} \tag{20}$$

$$U_n \approx \frac{-16 V_0 L\lambda^2}{\pi^3 H \sinh(n\pi H/L)} \sum_{m=1,3,...} \frac{\tanh(m\pi H/L)}{m(m^2-n^2)} \tag{21}$$

The electric field can be derived from the potential $E_x = -\frac{\partial V}{\partial x}$ and $E_y = -\frac{\partial V}{\partial y}$, which can then be used to calculate the current densities in eq. 5 (as well as the power dissipation density $p = \mathbf{E} \cdot \mathbf{J}$). The net current and total resistance are subsequently derived in app. A.

The voltage probes ΔV_1 and ΔV_2 indicated in fig. 2 are used to determine the transverse voltage drop, where the average, normalized voltage difference of both pairs is used as performance metric for the anisotropy. Probes at $y = \pm H/3$, $x = 0$ and $x = L$ are used for robust measurements, theoretically yielding:

$$\frac{\Delta V_{1/3}}{2V_0} = \frac{\Delta V_1 + \Delta V_2}{2 \cdot 2V_0} =$$
$$\frac{\left(V(L, \frac{H}{3}) - V(0, \frac{H}{3})\right) + \left(V(L, -\frac{H}{3}) - V(0, -\frac{H}{3})\right)}{2 \cdot 2V_0} =$$
$$\frac{\lambda L}{2H} - \frac{1}{V_0} \sum_{m=1,3,...} T_m \cosh\left(\frac{m\pi}{L}\frac{H}{3}\right) = \lambda \cdot f(H, L) \tag{22}$$

This shows that the measured $\Delta V_{1/3}/2V_0$ is proportional to $\tan(\theta_b)$ times a geometric term that only depends on H and L (to the order λ^2 accuracy), where the sign of $\Delta V_{1/3}/2V_0$ and λ are coupled through the odd function $\sin(\phi)\cos(\phi)$:

$$\frac{\Delta V_{1/3}}{2V_0} = \lambda \cdot f(H, L) = \tan(\theta_b) \cdot f(H, L) \tag{23}$$

The definition of the redirection angle in eq. 11 is consistent with the definition of Tarkhanyan et al. [40], who showed that both β and ϕ can be used to optimize the anisotropy (where the coordinate system of Tarkhanyan is rotated with respect to the definition in this paper):

$$\phi_{\max} = \pi/2 - \arctan\left(\sqrt{1+\beta}\right) \tag{24}$$

$$|\theta_{\max}| = \arctan\left(\frac{\beta}{2\sqrt{1+\beta}}\right) \tag{25}$$

This means that the only parameters required to tune the DC electric metamaterial effects are ϕ, ρ, σ and W and that the effect can directly be measured via the voltage probes and the total resistance. Furthermore the optimization of the anisotropy and total resistance can be done separately as long as the contact properties can be tuned, since the material choice fixes ρ and the process parameters determine W and σ.

The above model is based on the effective medium approximation, however in reality the medium consists of printed traxels with interfaces. To validate how big the difference is when assuming a smooth gradient instead of jumps across the interfaces, a voltage deviation expression based on the work of Vemuri et al. on thermal metamaterials is introduced [49]. It determines the average voltage deviation between a homogenized medium and a layered medium for the case where $\phi = 90°$ (this is the case with the largest jumps in voltage). The derivation for the unrotated DC electric metamaterial in app. C yields:

$$V_{\text{dev}} = \frac{\sigma/W}{\rho + \sigma/W} \frac{W}{2}\nabla V = \frac{\beta}{1+\beta}\frac{V_0}{N} \tag{26}$$

In case $\beta >> 1$ the voltage drops only occur across the interfaces and the deviation is the maximum value, for $\beta << 1$ and $N >> 1$ the deviation becomes insignificant. With the model and theoretical framework in place, the methodology for simulations and experiments can be introduced.

III. METHODOLOGY

A. Fabrication

The samples are single sheets fabricated with a Prusa i3 mk3s printer with a $0.4\,\text{mm}$ nozzle, combined with PrusaSlicer for slicing. As material ProtoPasta conductive PLA with a diameter of $1.75\,\text{mm}$ is used [50]. This material has a reported resistivity of $0.06\,\Omega\,\text{m}$ to $0.34\,\Omega\,\text{m}$, depending on the print settings and geometry [44], [51]–[53]. The samples are squares of 30 x 30 x 0.2 mm, printed on top of oxidized silicon wafers, where a spray is used to improve adhesion (3DLAC). The electrical contacts are made with copper tape and silver paint (Electrolube SCP26G), having additional ridges on the outer ends of the samples to provide even contacts. For testing the effect of the print parameters on the anisotropy, prints are made with a $\phi = 45°$ infill angle, fig. 1.b, since this is the most optimal infill angle for low anisotropy ($\beta << 1$) in eq. 24. Two probing points are added symmetrically on either side for reliable voltage probing, fig. 1.b, where the average voltage difference of both pairs is used as measure for the skewed voltage distribution. Small and symmetrical sensing contacts are chosen for high sensitivity, inspired by pseudo-Hall effect measurements [54]. The prints are made with the default printing parameters from table I, while varying a single parameter at a time for T_{noz}, T_{bed} and W_{ext}. Furthermore the low and high parameter values where combined to test their joint effect, giving samples with $T_{\text{noz}} = 200\,°\text{C}$, $T_{\text{bed}} = 25\,°\text{C}$ and $W_{\text{ext}} = 0.4\,\text{mm}$; with the default parameters and with $T_{\text{noz}} = 230\,°\text{C}$, $T_{\text{bed}} = 70\,°\text{C}$ and $W_{\text{ext}} = 0.8\,\text{mm}$. A concentrator consisting of four versions of the sample in fig. 1.b combined is also fabricated as a DC electric metamaterial demonstration, on a glass and on a silicon wafer. The combined low printing parameter values are used to yield a large contact resistance and anisotropy and hence the best DC electric metamaterial properties.

B. Simulation

FEM simulations are used to study the model assumptions and experimental results. The simulations are performed with

TABLE I: Printing parameters.

Printing parameter	Default Value	Low and High Value
Bed temperature	50 °C	25 °C to 70 °C
Nozzle temperature	215 °C	200 °C to 230 °C
Extrusion width	0.6 mm	0.4 mm to 1.2 mm
Extrusion multiplier	1	-
Infill Density	100%	-
Infill angle	45°	-
Layer height	0.2 mm	-
Printing speed	20 mm s^{-1}	-

COMSOL Multiphysics 5.4 using the Electric Currents module with an extremely fine mesh. To verify the model, both simulations of the EMA model and a full traxel model with electrical contacts are performed. The electrical properties are implemented through the use of the electrical conductivity tensor $\hat{\kappa}_{\text{eff}}$ in eq. 5 (EMA case) and through material properties and contact impedance functionality (full traxel case), similar to [10], [19]. The meandering ends of the traxels are neglected, since these have a small effect for square samples with a relatively high Γ value [19]. The default geometric parameters in table I are used. A sweep is performed for the contact resistivity over a logarithmic range from $\sigma = 1 \times 10^{-8}\,\Omega\,\text{m}^2$ to $\sigma = 1\,\Omega\,\text{m}^2$ in powers of 10, while using $\rho = 0.221\,\Omega\,\text{m}$ after measuring it on a square sample along the print direction of the lines. To properly compare the simulations, the relative voltage difference and the total resistance are determined and the error of the model and EMA simulation with respect to the full traxel simulation are determined. Next the voltage and current density distributions can be compared. As an additional validation step, voltage data acquired with voltage contrast scanning electron microscopy (VCSEM) and an FEM simulation from earlier work are used [10] to show jumps in voltage across traxel interfaces. Furthermore the voltage over the centerline of samples is studied at $x = L/2$ and y runs from $-H$ to H. A mesh convergence study showed convergence of the voltage and total resistance for the used mesh size. Finally the concentrator demonstration is simulated to compare the power dissipation distribution and the centerline voltage to measurements by means of fitting σ.

C. Characterization

The voltage difference between opposite probe pairs and the resistance of the samples between the copper contacts are measured with a handheld digital multimeter (Fluke 175). The contact resistance for a typical sample was measured to be around $7\,\Omega$, which is negligible relatively to the total sample resistance. The measurements could therefore be performed with a two-wire resistance measurement. For every parameter, 2 or 3 samples are tested (in case of 2 instead of 3 samples, fabrication of a sample failed due to limited substrate adhesion). The analytical model shows that the voltage difference is a direct consequence of the anisotropic resistivity and is proportional to λ, and can therefore indeed be used as metric for the anisotropy. The cross-sections of samples with extreme parameters are imaged with a Keyence VHX-7000 microscope, where the cross-sections are prepared by cryo

fracturing with liquid nitrogen. The concentrator demonstration is investigated with IR thermography with an IR camera (FLIR ONE Gen 2, FLIR Systems) to show heating of the sample due to power dissipation. The temperature distribution is affected by thermal diffusion and convection. Furthermore the emissivity of the ProtoPasta surface is unknown and therefore the thermal imaging only serves as indicator for areas with high power density [10]. To show concentration of the current, probe voltage measurements are performed over the centerline of the concentrator with the multimeter.
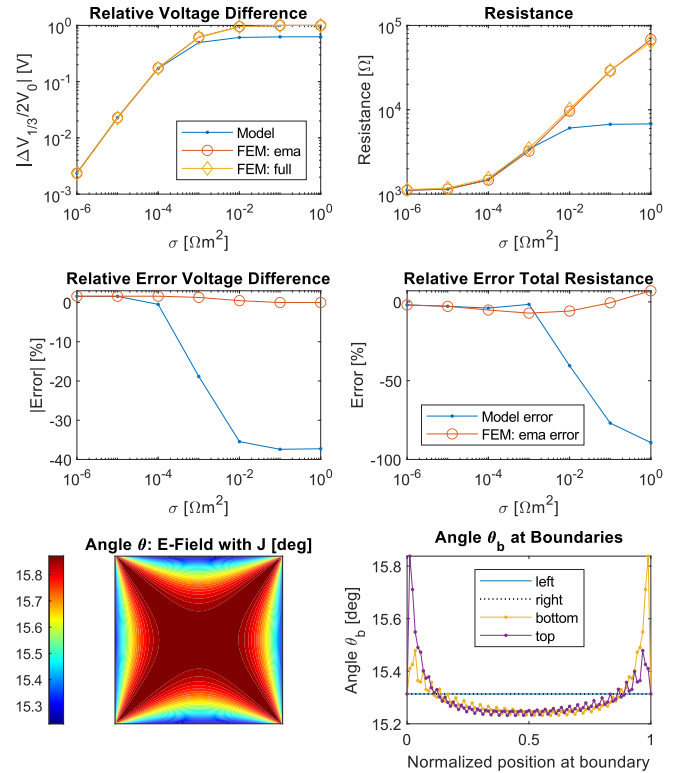
IV. RESULTS

A. Model Verification

Fig. 3: Comparison of the relative voltage difference and the total resistance as a function of the contact resistivity σ for both the model, EMA simulations and full FEM simulations (top). As well as the relative error of the voltage difference and the total resistance with respect to the full FEM simulations (center). For these parameters a value of $\sigma = 2.95 \times 10^{-5}\,\Omega\,\text{m}^2$ corresponds to $\lambda = -0.1$, and $\sigma = 1 \times 10^{-4}\,\Omega\,\text{m}^2$ to $\lambda = -0.274$. The angle θ was checked at the boundaries to verify the model (bottom). For $\sigma = 1 \times 10^{-4}\,\Omega\,\text{m}^2$ the angle starts deviating at the top and bottom boundary.

Fig. 3 presents the model and FEM results for the voltage difference and total resistance and their error with respect to the full traxel simulation. Both the resistance and voltage difference increase with σ for all cases, where the normalized voltage difference converges to 1. After $\sigma > 1 \times 10^{-4}\,\Omega\,\text{m}^2$ the model starts to deviate from the full simulations, due to neglecting the $-2\lambda \frac{\partial^2 V}{\partial x \partial y}$ term. This term becomes dominant

for large $|\lambda|$, which in particular affects the total resistance. For values of $\lambda = -0.1$ ($\sigma = 2.95 \times 10^{-5}\,\Omega\,\mathrm{m}^2$) the model is still valid as expected. Even up to $\lambda \approx -0.274$ ($\sigma = 1 \times 10^{-4}\,\Omega\,\mathrm{m}^2$) the model results are still within $9\,\%$ for the voltage error and $6.2\,\%$ for the total resistance error. The EMA simulations closely follow the full traxel simulations for the entire simulated range, indicating that the homogenization is valid for the used number of traxels. Finally the angle θ_b at the boundaries was also used for verification, since it starts deviating when the model assumptions break done, as shown at the bottom in fig. 3.

The simulated centerline voltages for various values of σ can be seen in fig. 4. The voltage jumps in the full traxel case become clear compared to the smooth EMA simulations. Furthermore a larger σ yields a more nonlinear voltage distribution. The insert shows the average voltage difference between EMA and full traxel simulations for $\phi = 90°$ (like in fig. 10, for other angles the deviation becomes smaller). From this it becomes clear that, despite the difference in continuity, both simulations show the same general trend, where the deviation is relatively small.
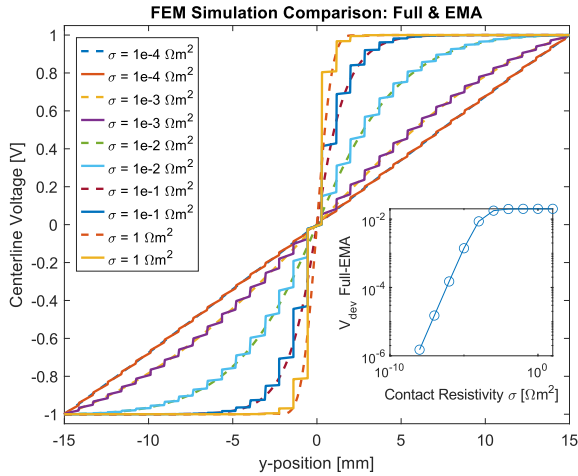

Fig. 4: EMA (dotted lines) and full traxel FEM simulations (continuous lines) of the voltage on the centerline, $x = L/2$ and y from $-H$ to H. Data for $\sigma = 1 \times 10^{-4}\,\Omega\,\mathrm{m}^2$ to $\sigma = 1\,\Omega\,\mathrm{m}^2$ is plotted, where larger σ yield a bigger deviation from a linear curve. In the insert, a graph illustrating the theoretical voltage deviation between EMA and full simulation from eq. 26 as function of contact resistivity for $\phi = 90°$ is presented ($V_{\mathrm{dev}} \approx 0.0014\,\mathrm{V}$ for $\sigma = 1 \times 10^{-5}\,\Omega\,\mathrm{m}^2$).

Discontinuous voltage jumps across interfaces can also be found in literature [55] and in measurement data. Fig. 5 shows voltage data compared to FEM simulations with voltage jumps across interfaces for previous data [10].

Finally the voltage and current density norm distributions from the model and both simulations are compared for $\sigma = 1 \times 10^{-4}\,\Omega\,\mathrm{m}^2$ in fig. 6. All three cases show similar distributions. It should be noted that for large values of λ the modeled voltage has as significant error around the top and bottom edge due to neglecting the mixed derivative term: $-2\lambda \frac{\partial^2 V}{\partial x \partial y}$. This term is at its biggest there, since the the electric field
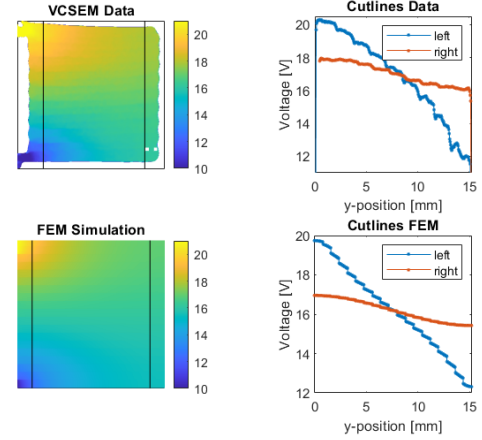

Fig. 5: Measured voltage data compared to FEM simulations that show discontinuous jumps in voltage between neighbouring traxels, data adapted from [10]. The voltage graphs on the right present data of the black cut lines.

changes the most in both x and y-direction around the top and bottom (as shown by Moelter et al. [45]). Besides that, there is a difference in peak current density between all cases in the bottom left and top right corners which is likely caused by the homogenization. Finally in the full traxel simulations jumps in voltage and current density can be seen, caused by the discrete interfaces.

B. Measurement Data

The mean results for the normalized voltage difference between the probes and the total resistance of the samples with the first standard deviation are shown in fig. 7, where every parameter has its own horizontal axis. As expected the voltage difference, and hence the anisotropy, goes down with increasing T_{noz}, T_{bed} and W_{ext}, indicating a decrease in contact resistance. The total resistance also goes down with an increase of these parameters, as already found in [9], [44]. This holds for all values except for the highest T_{noz} and T_{bed}, which does not have an explanation yet. The combined parameter data shows a similar trend, where a bigger voltage difference was achieved for the combined low parameters. From the voltage difference λ was estimated with the model (the proportionality constant in eq. 23 solely depends on geometry, $f \approx 0.636$). The model is only valid for low $|\lambda|$, and for combined high printing parameters $\lambda = -0.119$. This yields estimated values of $\rho = 0.222\,\Omega\,\mathrm{m}$ and $\sigma = 4.80 \times 10^{-5}\,\Omega\,\mathrm{m}^2$ with $\Gamma = 0.787$.

The cross-sections of samples are examined with microscopy to check if the anisotropy can be caused by contact properties, fig. 8. For the low T_{noz}, an interface between both traxels is present that likely indicates limited fusion. For high values the cross-sections appear solid. For some parameters the prints have ridges or gutters, this over and under-extrusion will also have an effect on the anisotropy.

C. Concentrator Demonstration

The most effective parameters from fig. 7 are used for printing the concentrator: $T_{\mathrm{noz}} = 200\,°\mathrm{C}$, $T_{\mathrm{bed}} = 25\,°\mathrm{C}$ and
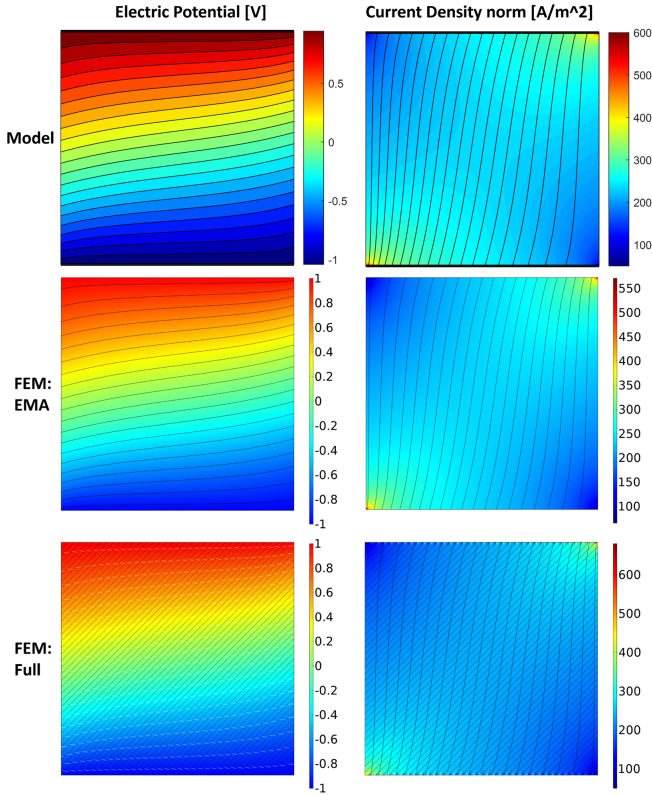
Fig. 6: Voltage and current density norm distributions for the model, the EMA simulation and the full traxel simulation with $\sigma = 1 \times 10^{-4}\,\Omega\,\mathrm{m}^2$. The global trends are the same for all cases, however locally the equipotential curves and the current density in the full simulation show discontinuous jumps due to the resistive interfaces.

$W_{\mathrm{ext}} = 0.4\,\mathrm{mm}$. The concentrator in fig. 9.a is measured with IR thermography, fig. 9.b and shows qualitatively comparable results to FEM simulations of the power dissipation density in fig. 9.c, showing its operation with heating mainly on the corners and in the center of the concentrator (with a limited maximum value in the colour scale to match the spread out temperature distribution due to thermal conduction [10]). The bright spot in the lower left corner in the thermal image is caused by a solder joint which reflects the surrounding IR.

The probe voltage measurements over the centerline in fig. 9.d also show a higher voltage gradient in the center compared to a linear voltage drop for isotropic materials, demonstrating the concentrating effect. The FEM simulations are fitted to the measurements, yielding a $\Gamma = 0.570$ (Si) and $\Gamma = 0.307$ (glass), comparable to the anisotropy ratio of $\Gamma = 0.528$ in [10]. The difference between the samples on the glass and silicon wafers might be explained from the different thermal properties of the substrates, affecting bond formation.

V. DISCUSSION AND CONCLUSION

The methodology and results present various points for discussion. The homogenization in the model is verified by means of FEM simulations. The comparison shows that the homogenization locally introduces errors in the electric field,
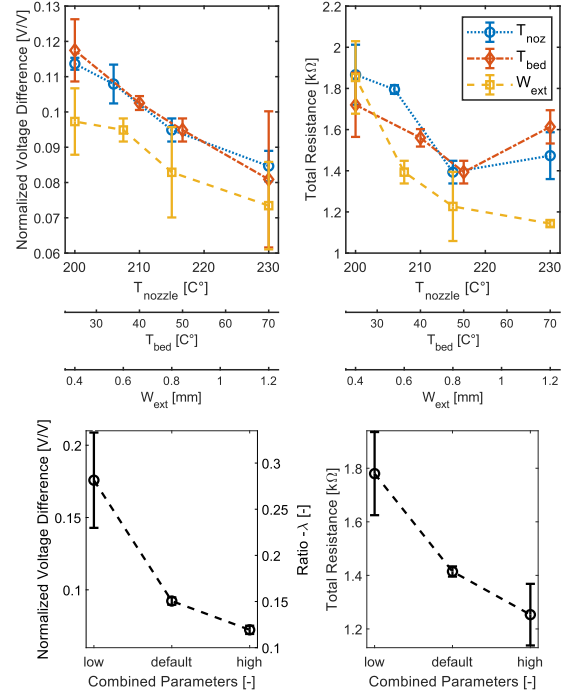

Fig. 7: The measured mean normalized voltage difference (left) and total resistance (right) with their standard deviation as a function of the parameters T_{noz}, T_{bed} and W_{ext} on the top, where each parameter has an own horizontal axis. On the bottom the measured voltage difference (and modeled λ) and total resistance for the samples with combined parameters.
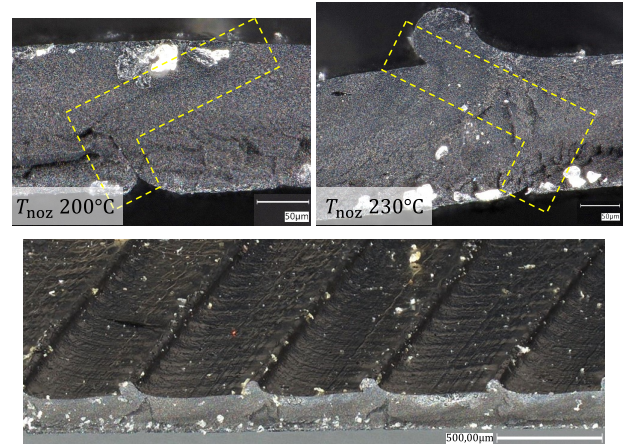

Fig. 8: Microscopy images of cross-sections from samples with extreme nozzle temperature (top) and a full sample view (bottom). The low temperature shows a ridge at the traxel interface encircled by the yellow box compared to the fully fused contacts at high temperature, which indicates reduced bonding formation. The light areas are silver flakes from electrical contact paint contamination.

since in the bulk material with interfaces $\mathbf{E}$ and $\mathbf{J}$ are always aligned. As a consequence the constant value of the redirection angle θ_{b} in eq. 11 only exists in the EMA model and not in the real traxel case. However, this does not cause significant
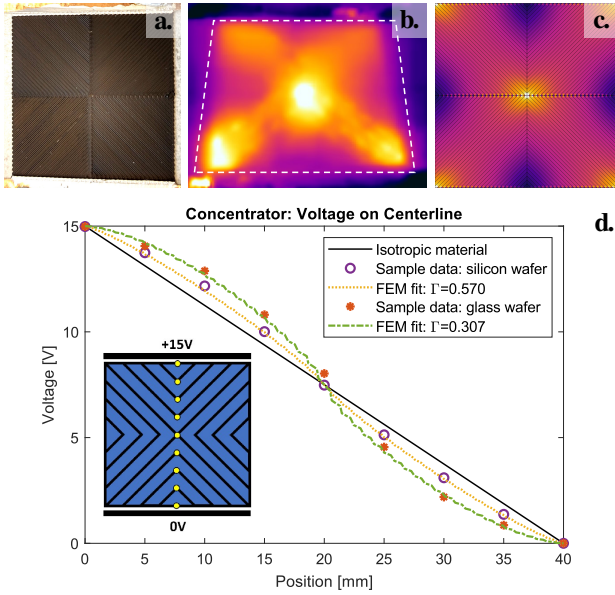
Fig. 9: **a.** The fabricated concentrator on a glass substrate. **b.** An IR image of the concentrator in operation, mainly showing heating at the center and in the corners (the hot spot in the lower left corner is a reflecting solder joint). **c.** An FEM simulation of the power dissipation density with a clipped colour scale, showing similarity to the IR measurement. **d.** The measured voltage and fitted simulations over the centerline of the fabricated concentrators, demonstrating its operation with a higher electric field in the middle. The concentrator is schematically shown on the left, with the dots representing the probe locations.

problems for anisotropy as well as for the voltage difference and the total resistance since they are no local properties. As shown with eq. 26, the voltage deviation is small and the errors between the EMA and full FEM simulation are small as well. Evenmore, the jumps in voltage across interfaces were also found in experimental data. The meandering traxel ends, as seen in fig. 2, are neglected in both the model and simulations, since their effect is small for square samples with low anisotropy [10]. The model assumptions also require low anisotropy, due to approximating T_m and U_n up to the order λ^2 and neglecting the transverse conductivity component in eq. 16. The results in fig. 3 show that the model is reliable for the voltage difference and total resistance up to $\sigma = 1 \times 10^{-4}\,\Omega\,\mathrm{m}^2$ or $\lambda = -0.274$, although it does start to show errors in the angle at the boundaries, fig. 3. The model is not limited to the used aspect ratio and can be used for other DC metamaterials that are described by a Laplace equation, e.g. in thermostatics [25], magnetostatics [56] and specific hydrodynamics [57]. For low $|\lambda|$ values the model can be used as characterization method to determine the resistivity ρ and contact resistivity σ, where the found value of $\rho = 0.222\,\Omega\,\mathrm{m}$ is similar to an earlier measured and reported value [44]. On the other hand the highest achieved anisotropy ratio for the concentrator on glass was $\Gamma = 0.306$, which corresponds to values of $\beta = 2.27$ and $|\lambda| = 0.531$. The lowest value of λ for the combined high temperatures and wide traxels was

found to be $|\lambda| = 0.119$, which corresponds to $\beta = 0.270$. Hence β was varied from 0.270 to 2.27, from a dominant ρ with little DC electric metamaterial behaviour to a dominant σ with significant DC electric metamaterial behaviour. This achievable range of β makes the practical application of the DC electric metamaterial behaviour possible.

A limited set of printing parameters is studied, namely T_{noz}, T_{bed} and W_{ext}, which can even be combined to achieve more anisotropy. There also seems to be an interplay between the parameters, e.g. both a high T_{noz} and T_{bed} does not give double the effect. A more extensive parameter space should be studied to determine the interaction terms. Contrary to these results, Daniel et al. showed that temperatures and print speed do not affect the anisotropy in vertical walls, but only the absolute resistance [11]. This can possibly be explained from Daniel et al. only studying vertical walls, whereas this work uses single horizontal layers. Watschke et al. also demonstrated the effect of tuning the printing speed and extrusion multiplier on the resistivity [44], Stankevich et al. used annealing to lower the effective resistivity [51] and Mousavi et al. showed the effect of infill density on the contact resistance (even going up to $\sigma = \infty$ with air gaps) [13], which can be tested as additional tuning possibilities. Finally Tarkhanyan et al. demonstrated the use of ϕ for optimizing the anisotropy, eq. 24. Furthermore it was observed that extreme printing settings can weaken the 3D-prints mechanically and make it more difficult to print. Printing with dual materials could remedy this aspect, allowing for improved mechanical performance. This changes the resistivity tensor to the derivation in app. B. It also allows for more design freedom in 3D, since it can be challenging to move from 2D to 3D geometries for layered DC metamaterials [37]. In this respect additive manufacturing can open up pathways to 3D DC metamaterials [58], e.g. through 5-axis printing [59]. Evenmore, the findings also hold merit for other material extrusion-based printing methods similar to FFF, such as Direct Ink Writing (DIW), as well as other layered materials, such as CFRP.

To improve measurements a full voltage surface-based measurement like VCSEM in fig. 5 could be more useful, instead of only measuring the voltage with four probes. However this only works for very small surfaces. A promising alternative is a probe scanning method for conductive 3D-prints [55]. The microscopy images show the contact interface for low T_{noz}, where the contact appears bigger than just a vertical cross-section. The images provide an indication of improper fusion, however additional research is required for a better understanding of the bond formation and the root cause of the contact resistance [11].

All-in-all this work experimentally proves that decreasing the nozzle temperature, bed temperature and extrusion width can be used to increase the contact resistance, to achieve anisotropic electrical conduction with FFF in single layer prints. The temperatures influence the contact resistivity between printed lines, whereas the extrusion width determines the number of interfaces per unit length. Combining these parameters gives an increased anisotropy effect. The presented effective medium model reliably describes the DC electric metamaterial behaviour for low anisotropy, giving

reference and input for characterizing and optimizing the anisotropy, respectively. The measurement method inspired by the pseudo-Hall effect allows for reliably measuring the anisotropy. Through microscopy observations it is validated that the printing parameters indeed influence the quality of the contacts between printed lines. The anisotropy is used for DC electric metamaterials, which are interesting for electronics, sensors, actuators and heaters e.g. by concentrating the current to increase sensitivity. Such a concentrator is 3D-printed and its operation is demonstrated through IR thermography and voltage measurements as well as compared with FEM simulations. In conclusion, realization of DC electric metamaterials with FFF is presented as an additional tool in the design toolbox for 3D-printing of electrical conductors.

APPENDIX A
CURRENT AND RESISTANCE DERIVATION

The net current can be found by integrating J_y in eq. 5 over a horizontal section of thickness t:

$$I_y = t \int_0^L J_y \, dx = t \int_0^L \left(\kappa_{yx} E_x + \kappa_{yy} E_y \right) dx =$$

$$t \left(\kappa_{yx} \left(\frac{V_0 L}{H} \lambda - 2 \sum_{m=1,3,...} T_m \right) + \kappa_{yy} \frac{V_0 L}{H} \right) =$$

$$t\kappa_{yy} \left(\frac{V_0 L}{H} - \lambda \left(\frac{V_0 L}{H} \lambda - 2 \sum_{m=1,3,...} T_m \right) \right) \quad (27)$$

For $\phi = 0$ (and hence $\lambda = 0$ and $\kappa_{yy} = 1/\rho$) the current reduces to $I_y = \frac{V_0 t L}{H \rho}$, which is the expected current for an isotropic plate. From the current, the total resistance can be calculated:

$$R = \frac{2V_0}{I_y} \quad (28)$$

APPENDIX B
DUAL MATERIAL MODEL WITH INTERFACES

To obtain more design freedom for creating anisotropy, the principles of creating anisotropy by means of dual materials and by means of resistive interfaces can be combined. This results in the following effective resistivity tensor, with W_1 and W_2 as traxel widths and ρ_1 and ρ_2 as resitivity for both materials:

$$\hat{\rho}_{\text{eff}} = \begin{bmatrix} \rho'_{xx} & 0 \\ 0 & \rho'_{yy} \end{bmatrix} \quad (29)$$

$$\rho'_{xx} = \frac{W_1 \rho_1 + W_2 \rho_2 + 2\sigma}{W_1 + W_2} \quad (30)$$

$$\rho'_{yy} = \frac{(W_1 + W_2)\rho_1 \rho_2}{W_2 \rho_1 + W_1 \rho_2} \quad (31)$$

When simplifying this to $W_1 = W_2 = W$ and an infill angle of $\phi = 45°$, λ in eq. 8 reduces to:

$$\lambda \Big|_{\phi=45°} = \frac{\rho'_{yy} - \rho'_{xx}}{\rho'_{xx} + \rho'_{yy}} = \frac{\left(\frac{2\rho_1\rho_2}{\rho_1+\rho_2} - \frac{(\rho_1+\rho_2)}{2} - \frac{\sigma}{W} \right)}{\frac{(\rho_1+\rho_2)}{2} + \frac{\sigma}{W} + \frac{2\rho_1\rho_2}{\rho_1+\rho_2}} \quad (32)$$

Combining these two effects, gives the freedom to also design for other requirements, e.g. thermal or mechanical properties.

APPENDIX C
VOLTAGE DEVIATION IN THE EFFECTIVE MEDIUM APPROXIMATION

The average voltage deviation between a layered medium and the effective medium approximation can be expressed for the case where $\phi = 90°$, fig. 10 on the right. This derivation is based on the work of Vemuri et al. for the thermal case, where the graph in fig. 10 illustrates the voltage profiles. The voltage deviation is defined as the average voltage difference between the linear profile of the effective medium approximation ($\Delta V_{\text{EMA}} = \frac{\rho W + \sigma}{A} I$) and the discontinuous profile of the layered medium with bulk resistance ($\Delta V_{\text{bulk}} = \frac{\rho W}{A} I$) and contact resistance ($\Delta V_{\text{contact}} = \frac{\sigma}{A} I$), for current I and cross-sectional area A:

$$V_{\text{dev}} = \frac{\text{Total area enclosed by triangles}}{\text{Length of sample}} \quad (33)$$

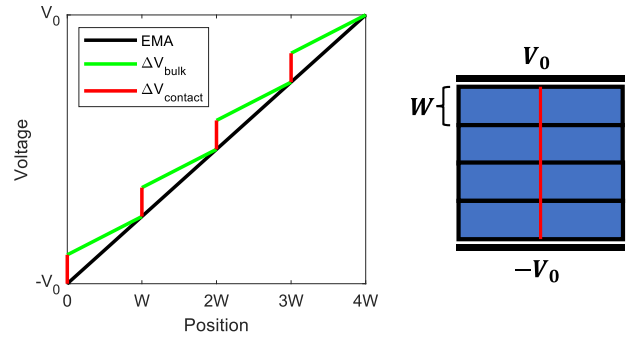$$= \frac{\sigma/W}{\rho + \sigma/W} \frac{W}{2} \nabla V = \frac{\beta}{1+\beta} \frac{V_0}{N} \quad (34)$$

Fig. 10: Voltage profiles for effective medium approximation versus fully simulated case, adapted from [49]. The lay-out with $\phi = 90°$ is shown on the right.

REFERENCES

[1] A. Dijkshoorn, T. Hamstra, R. Sanders, S. Stramigioli, and G. Krijnen, "DC electric metamaterial behaviour in tuned fused deposition modelling prints," in *2021 IEEE Sensors*, 2021.

[2] Y. Xu *et al.*, "The boom in 3d-printed sensor technology," *Sensors*, vol. 17, no. 5, 2017.

[3] A. Dijkshoorn *et al.*, "Embedded sensing: integrating sensors in 3-d printed structures," *JSSS*, vol. 7, no. 1, 2018.

[4] M. Schouten, G. Wolterink, A. Dijkshoorn, D. Kosmas, S. Stramigioli, and G. Krijnen, "A review of extrusion-based 3d printing for the fabrication of electro- and biomechanical sensors," *IEEE Sens. J.*, vol. 21, no. 11, 2021.

[5] N. Lazarus and H. H. Tsang, "3-d printing structural electronics with conductive filaments," *IEEE Trans. Compon. Packag. Manuf.*, vol. 10, no. 12, 2020.

[6] D. V. Baker, C. Bao, and W. S. Kim, "Highly conductive 3d printable materials for 3d structural electronics," *ACS Appl. Electron. Mater.*, vol. 3, no. 6, 2021.

[7] B. Hampel, S. Monshausen, and M. Schilling, "Properties and applications of electrically conductive thermoplastics for additive manufacturing of sensors," *Technisches Messen*, vol. 84, no. 9, 2017.

[8] N. Lazarus and S. S. Bedair, "Creating 3d printed sensor systems with conductive composites," *Smart Mater. Struct.*, vol. 30, no. 1, 2020.

[9] J. Zhang *et al.*, "Resistivity and its anisotropy characterization of 3d-printed acrylonitrile butadiene styrene copolymer (abs)/carbon black (cb) composites," *Appl. Sci.*, vol. 7, no. 1, 2017.

[10] A. Dijkshoorn *et al.*, "Characterizing the electrical properties of anisotropic, 3d-printed conductive sheets for sensor applications," *IEEE Sens. J.*, vol. 20, no. 23, 2020.

[11] F. Daniel, A. Gleadall, and A. D. Radadia, "Influence of interface in electrical properties of 3d printed structures," *Addit. Manuf.*, vol. 46, 2021.

[12] D. Pejak Simunec and A. Sola, "Emerging research in conductive materials for fused filament fabrication: A critical review," *Adv. Eng. Mater.*, vol. 24, no. 7, 2022.

[13] S. Mousavi, D. Howard, F. Zhang, J. Leng, and C. H. Wang, "Direct 3D Printing of Highly Anisotropic, Flexible, Constriction-Resistive Sensors for Multidirectional Proprioception in Soft Robots," *ACS Applied Mater. Interfaces*, vol. 12, no. 13, 2020.

[14] G. Wolterink, R. Sanders, and G. Krijnen, "Thin, flexible, capacitive force sensors based on anisotropy in 3d-printed structures," in *2018 IEEE SENSORS*, 2018.

[15] L. Truman, E. Whitwam, B. Nelson-Cheeseman, and L. Koerner, "Conductive 3d printing: resistivity dependence upon infill pattern and application to emi shielding," *J. Mater. Sci.: Mater. Electron.*, vol. 31, 2020.

[16] L. Guadagno *et al.*, "Electrical anisotropy controlled heating of acrylonitrile butadiene styrene 3d printed parts," *Mater. Des.*, vol. 225, 2023.

[17] C. J. Hohimer, G. Petrossian, A. Ameli, C. Mo, and P. Pötschke, "3d printed conductive thermoplastic polyurethane/carbon nanotube composites for capacitive and piezoresistive sensing in soft pneumatic actuators," *Addit. Manuf.*, vol. 34, 2020.

[18] F. Califano, A. Dijkshoorn, S. Roodink, S. Stramigioli, and G. Krijnen, "Energy-aware control of euler–bernoulli beams by means of an axial load," *IEEE/ASME Trans. Mechatron.*, vol. 27, no. 6, 2022.

[19] A. Dijkshoorn, M. Schouten, S. Stramigioli, and G. Krijnen, "Modelling of anisotropic electrical conduction in layered structures 3d-printed with fused deposition modelling," *Sensors*, vol. 21, no. 11, 2021.

[20] C. Navau *et al.*, "Enhancing the sensitivity of magnetic sensors by 3d metamaterial shells," *Sci. Rep.*, vol. 7, 2017.

[21] H. Barati Sedeh, M. Fakheri, A. Abdolali, and F. Sun, "Experimental demonstration of an arbitrary shape dc electric concentrator," *Sci. Rep.*, vol. 10, no. 1, 2020.

[22] T. Yang *et al.*, "Invisible sensors: Simultaneous sensing and camouflaging in multiphysical fields," *Adv. Mat.*, vol. 27, no. 47, 2015.

[23] T. Han and C.-W. Qiu, "Transformation laplacian metamaterials: recent advances in manipulating thermal and dc fields," *J. Opt.*, vol. 18, no. 4, 2016.

[24] M. Kadic, T. Bückmann, R. Schittny, and M. Wegener, "Metamaterials beyond electromagnetism," *Rep. Prog. Phys.*, vol. 76, no. 12, 2013.

[25] P. R. Bandaru, K. P. Vemuri, F. M. Canbazoglu, and R. S. Kapadia, "Layered thermal metamaterials for the directing and harvesting of conductive heat," *AIP Adv.*, vol. 5, no. 5, 2015.

[26] F. M. Canbazoglu, K. P. Vemuri, and P. R. Bandaru, "Estimating interfacial thermal conductivity in metamaterials through heat flux mapping," *Appl. Phys. Lett.*, vol. 106, no. 14, 2015.

[27] X. Zheng and B. Li, "Effect of interfacial thermal resistance in a thermal cloak," *Phys. Rev. Applied*, vol. 13, 2020.

[28] T. Chen and J.-H. Lin, "Novel connections and physical implications of thermal metamaterials with imperfect interfaces," *Sci. Rep.*, vol. 12, no. 1, 2022.

[29] ——, "Exact thermal invisibility for spherical cloaks with imperfect interfaces," *AIP Adv.*, vol. 12, no. 7, 2022.

[30] W. Jiang, C. Luo, H. Ma, Z. Mei, and T. Cui, "Enhancement of current density by dc electric concentrator," *Sci. Rep.*, vol. 2, 2012.

[31] F. Yang, Z. Mei, T. Jin, and T. Cui, "Dc electric invisibility cloak," *Phys. Rev. Lett.*, vol. 109, no. 5, 2012.

[32] T. Han *et al.*, "Manipulating dc currents with bilayer bulk natural materials," *Adv. Mat.*, vol. 26, no. 21, 2014.

[33] M. Hou *et al.*, "Fast-printed laser-induced-graphene pattern enabling directional thermal manipulation," *Int. J. Heat Mass Transf.*, vol. 197, 2022.

[34] M. Askari *et al.*, "Additive manufacturing of metamaterials: A review," *Addit. Manuf.*, vol. 36, 2020.

[37] J. Fan *et al.*, "A review of additive manufacturing of metamaterials and developing trends," *Mater. Today*, vol. 50, 2021.

[35] X. Wu, Y. Su, and J. Shi, "Perspective of additive manufacturing for metamaterials development," *Smart Mater. Struct.*, vol. 28, no. 9, 2019.

[36] T. Koschny, C. M. Soukoulis, and M. Wegener, "Metamaterials in microwaves, optics, mechanics, thermodynamics, and transport," *J. Opt.*, vol. 19, no. 8, 2017.

[38] F. Magnus, B. Wood, J. Moore, K. Morrison, G. Perkins, J. Fyson, M. Wiltshire, D. Caplin, L. Cohen, and J. Pendry, "A d.c. magnetic metamaterial," *Nature Materials*, vol. 7, no. 4, p. 295 – 297, 2008.

[39] G. Park, S. Kang, H. Lee, and W. Choi, "Tunable multifunctional thermal metamaterials: Manipulation of local heat flux via assembly of unit-cell thermal shifters," *Sci. Rep.*, vol. 7, 2017.

[40] R. H. Tarkhanyan and D. G. Niarchos, "Geometrically Tunable Transverse Electric Field in Multilayered Structures," *Adv. in Condensed Matter Phys.*, vol. 2017, 2017.

[41] G. Stano, A. Di Nisio, A. Lanzolla, M. Ragolia, and G. Percoco, "Fused filament fabrication of commercial conductive filaments: experimental study on the process parameters aimed at the minimization, repeatability and thermal characterization of electrical resistance," *Int. J. Adv. Manuf. Technol.*, vol. 111, no. 9-10, 2020.

[42] C. Bellehumeur, L. Li, Q. Sun, and P. Gu, "Modeling of bond formation between polymer filaments in the fused deposition modeling process," *J. Manuf. Process.*, vol. 6, no. 2, 2004.

[43] N. Polychronopoulos and J. Vlachopoulos, "The role of heating and cooling in viscous sintering of pairs of spheres and pairs of cylinders," *Rapid Prototyp. J.*, vol. 26, no. 4, 2020.

[44] H. Watschke, K. Hilbig, and T. Vietor, "Design and characterization of electrically conductive structures additively manufactured by material extrusion," *Appl. Sci.*, vol. 9, no. 4, 2019.

[45] M. J. Moelter, J. Evans, G. Elliott, and M. Jackson, "Electric potential in the classical hall effect: An unusual boundary-value problem," *Am. J. Phys.*, vol. 66, no. 8, 1998.

[46] H. Shibata and R. Terakado, "Resistance value and field distribution of rectangular anisotropic resistive region," *Electron. Lett.*, vol. 19, no. 14, 1983.

[47] N. Athanasopoulos and V. Kostopoulos, "A comprehensive study on the equivalent electrical conductivity tensor validity for thin multidirectional carbon fibre reinforced plastics," *Compos. B: Eng.*, vol. 67, 2014.

[48] U. Ausserlechner, "An analytical theory of piezoresistive effects in hall plates with large contacts," *Adv. in Condensed Matter Phys.*, 2018.

[49] K. P. Vemuri and P. R. Bandaru, "Geometrical considerations in the control and manipulation of conductive heat flux in multilayered thermal metamaterials," *App. Phys. Lett.*, vol. 103, no. 13, 2013.

[50] ProtoPlant, "Electrically Conductive Composite PLA." [Online]. Available: https://www.proto-pasta.com/products/conductive-pla

[51] S. Stankevich *et al.*, "Electrical resistivity of 3d-printed polymer elements," *Polymers*, vol. 15, no. 14, 2023.

[52] F. Daniel, N. H. Patoary, A. L. Moore, L. Weiss, and A. D. Radadia, "Temperature-dependent electrical resistance of conductive polylactic acid filament for fused deposition modeling," *Int. J. Adv. Manuf. Technol.*, vol. 99, no. 5-8, 2018.

[53] M. Arh, J. Slavič, and M. Boltežar, "Experimental identification of the dynamic piezoresistivity of fused-filament-fabricated structures," *Addit. Manuf.*, vol. 36, 2020.

[54] M. Doelle, D. Mager, P. Ruther, and O. Paul, "Geometry optimization for planar piezoresistive stress sensors based on the pseudo-hall effect," *Sens. Actuators A: Phys.*, vol. 127, no. 2, 2006.

[55] M. Schouten and G. Krijnen, "Characterization of 3d printed sheets using multi-frequency scanning impedance microscopy," in *2021 IEEE Sensors*, 2021.

[56] R. H. Tarkhanyan and D. G. Niarchos, "Re-direction of dc magnetic flux in magnetically isotropic multilayered structures," *J. Magn. Magn. Mater.*, vol. 410, 2016.

[57] B. Wang and J. Huang, "Hydrodynamic metamaterials for flow manipulation: Functions and prospects," *Chin. Phys. B*, vol. 31, no. 9, 2022.

[58] M. Kadic, G. W. Milton, M. van Hecke, and M. Wegener, "3d metamaterials," *Nat. Rev. Phys.*, vol. 1, no. 3, 2019.

[59] F. Hong, B. Lampret, C. Myant, S. Hodges, and D. Boyle, "5-axis multimaterial 3d printing of curved electrical traces," *Addit. Manuf.*, vol. 70, 2023.